Experimental study of classical heat transport in a magnetized plasma

A. T. Burke, J. E. Maggs, and G. J. Morales
Department of Physics and Astronomy, University of California, Los Angeles, California 90095

(Received 27 July 1999; accepted 25 October 1999)

A systematic study is made of the axial and transverse heat transport that arises when a microscopic temperature filament is generated, under controlled conditions, in a magnetized plasma of large dimensions. For early times and relatively small temperature gradients the study conclusively demonstrates the two-dimensional pattern characteristic of the classical theory based on Coulomb collisions. The full nonlinear dependence of the transverse and axial electron heat conductivities is sampled through temperature changes in the range $\delta T_e/T_e \sim 1-10$. The dependence on the confining magnetic field is explored over a factor of 3 ($\sim$ factor of 10 in transverse conductivity). It is found that under quiescent conditions, the observed behavior agrees with classical theory within the experimental uncertainties. However, over long times and/or for steep temperature gradients, fluctuations develop spontaneously and cause a significant departure from the predictions of the classical theory. © *2000 American Institute of Physics.* [S1070-664X(00)02602-1]

I. INTRODUCTION

The theoretical foundations for heat transport due to Coulomb collisions (i.e., classical transport) in magnetized plasmas were developed nearly fifty years ago.[1,2] Although the classical theory forms the basis for the design and planning of major experimental activities and is explained in established textbooks on the subject, it has been difficult to quantitatively document the predicted behavior in basic laboratory studies.

It is common for heat transport studies to yield transport rates that are enhanced by orders of magnitude (i.e., so-called anomalous transport) over the values predicted by classical theory, the extreme measure of anomaly for cross-field transport being the Bohm-diffusion coefficient.

The essence of heat transport in a magnetized medium is that it is inherently an anisotropic phenomenon. The classical electron thermal conductivity in the axial direction (along the confining magnetic field B_0) is given by

$$\kappa_{\parallel} = (3.16) n_e T_e \tau_e / m_e ,$$

and, in the transverse direction by

$$\kappa_{\perp} = (1.47) \kappa_{\parallel} (\Omega_e \tau_e)^{-2},$$

where n_e is the electron plasma density, T_e the electron temperature (in electron volts), m_e the electron mass, and the electron collision time $\tau_e = (3.44 \times 10^5) T_e^{3/2}/(n_e \lambda)$, with λ the Coulomb logarithm associated with the judicious cut-off of singularities (at large distances for binary-encounter formulations, or at short distances in collective descriptions). The unique features of classical transport that complicate laboratory studies are that $\kappa_{\parallel} \propto T_e^{5/2}$ while $\kappa_{\perp} \propto B_0^{-2} T_e^{-1/2}$, which results in a large degree of anisotropy, i.e., the time scale for axial transport is much shorter than for cross-field transport. The discrepancy in time scales prevents a clear study of the three-dimensional propagation of heat pulses in magnetized plasmas. As a consequence, the majority of the heat transport studies probe the phenomena only in the direction transverse to the confining magnetic field.

In designing an experiment that is capable of measuring the unique two-dimensional pattern characteristic of classical theory, one must overcome the large disparity in the axial and transverse rates. This requires a very long system (of length L) whose temperature is increased by a heat source of small transverse extent (of radius a). When the condition $(a/L) < 1.72(\Omega_e \tau_e)^{-1}$ is satisfied, the rate of radial energy loss across the surface of a heated filament exceeds the rate of axial loss through the ends, and the anisotropic nature of heat transport can be probed. The conditions in the present study are chosen to satisfy this criterion.

The present experimental study is conducted in the Large Plasma Device[3] (LAPD) at the University of California, Los Angeles. The dimensions of the ambient plasma generated in this device are such that for the purpose of the present investigation the plasma can be conceptually thought to be infinite in extent along the axial and transverse directions. The experiment consists of injecting a small electron beam whose modest parameters are chosen such that its role is just to provide a controlled heat source that extends axially over a limited region ($<10\%$ of the total device length). The concept behind the heat transport study consists of making measurements of the time evolution of the electron temperature at finely spaced points across the magnetic field at distant positions from the beam injector, i.e., we observe the spatio-temporal development of a heat plume embedded in a cold, infinite, magnetized plasma. Also, the results reported here pertain to predominantly quiescent conditions in which the spontaneous development of fluctuations do not play a significant role in the transport behavior. Indeed, we observe that by varying the plasma and source conditions it is possible to enter a regime in which fluctuations cause the transport to deviate significantly from the behavior predicted by classical theory. However, we defer a discussion of such phenomena to future detailed publications, and concentrate here on features germane to classical transport. Although the confinement device, the heat source and the plasma conditions used are ideal for the controlled study of heat transport at the microscopic level (the generated temperature filaments

have transverse scales comparable to the electron skin-depth) a drawback in this study is the lack of robust electron and ion ''thermometers'' capable of sampling changes at the millimeter-scale resolution required by the underlying physics, and with response times in the range of 1 μs, as is characteristic of the phenomena. To the best of our knowledge there are no diagnostic methods available at the present time that meet these demanding requirements. Consequently, our studies must rely on a judicious and consistent interpretation of information derived from Langmuir probe measurements. At every stage of this study we have labored to eliminate measurements and conclusions that do not meet the best consistency checks.

To arrive at a rigorous quantitative test of classical theory we have developed a two-dimensional, nonlinear, transport code with realistic boundary conditions.The code uses the theoretically predicted values for the heat conductivities $\kappa_{\|}$, $\kappa_{\perp}$. The test consists of the direct comparison of the spatio-temporal evolution of the electron temperature deduced from a consistent analysis of Langmuir probe data with the predictions of the code. It must be emphasized that this is a much more rigorous and demanding test of the theory than just measuring the ''local''transport coefficients for a prescribed temperature gradient. The present procedure tests the full nonlinear dependence of both $\kappa_{\|}$ and $\kappa_{\perp}$ on T_e (the heat changes the ambient value of T_e by a large amount), as well as the nontrivial two-dimensional pattern that evolves with time due to the interplay between radial and axial heat flows (i.e., simultaneous changes in axial and radial temperature gradients).

It is found that within the accuracy of the measurements and the inherent uncertainties in the experimental arrangements, the observations reported here are in excellent agreement with the predictions of the classical theory of heat transport. The predicted rise times, saturation and temporal evolution of the temperature plume are validated experimentally. The measured radial temperature profiles agree remarkably well with the predicted values. In addition, the scaling of the phenomena on the strength of the confining magnetic field is confirmed over a factor of 3 (a factor of 9 variation in $\kappa_{\perp}$). Again, we emphasize the key comparison made with the transport code because of the sizable change and the relative importance of axial and radial heat flow that results as B_0 is varied.

The manuscript is organized as follows. In Sec. II we describe the experimental setup and plasma conditions in which the heat transport studies are made. In Sec. III we describe the diagnostic methodology used. The transport code is explained in Sec. IV and key predictions of classical theory are elucidated. Experimental results and a comparison with predictions of classical theory are presented in Sec. V. Conclusions are found in Sec. VI.

II. EXPERIMENTAL SETUP

The heat transport studies are conducted in the Large Plasma Device[3] (LAPD) at the University of California, Los Angeles. A schematic of the experimental setup is shown in Fig. 1. The plasma is generated by electrons (primaries)

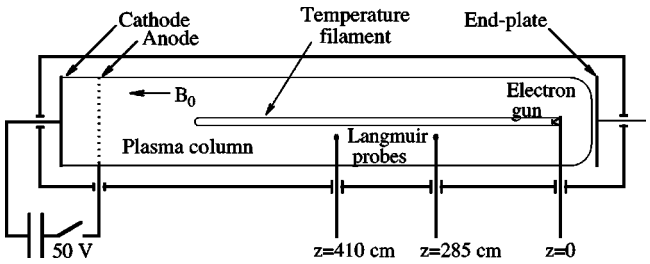

FIG. 1. Schematic of the experimental setup. A small (3 mm diameter) electron beam source is located near the end of the device away from the cathode. A low voltage beam (20 V) produces a heat source which creates a field-aligned, filamentary temperature plume. Planes of Langmuir probe data are taken at axial locations z_1 (285 cm) and z_2 (410 cm) far away from the heat source.

emitted from a heated, barium oxide coated cathode and subsequently accelerated by a semitransparent (transmission efficiency $\approx$50%) grid anode located 60 cm from the cathode. The end of the plasma column is terminated by an electrically floating copper plate. The accelerated primaries ($\sim$50 V) drift into a 9.4 m long vacuum chamber and strike neutral He gas at a fill pressure of 1.0×10^{-4} Torr to generate a 40 cm diameter, He plasma with a greater than 75% degree of ionization. Discharge currents of 1–5 kA are used to generate axially and radially uniform plasmas with measured densities $n_e=1.0$–$4.0\times10^{12}\,\mathrm{cm}^{-3}$, electron temperatures $T_e=6$–8 eV, and ion temperatures $T_i\simeq1$ eV. The confining magnetic field is varied in the range of 0.5–1.5 kG to test the predicted dependence of classical theory (i.e., $\kappa_{\perp}\propto B_0^{-2}$).

The heat transport studies are performed in the so-called afterglow phase of the plasma, i.e., after the discharge voltage pulse is terminated. Figure 2 illustrates the global time evolution of the discharge including the break down, steady-state, ramp-down, and afterglow stages. This figure shows the time evolution of the ion saturation current, I_{sat}, and the plasma density obtained with a 56 GHz interferometer. In the afterglow stage T_e decays rapidly (on a time scale of 100 μs) due to classical heat conduction to the ends of the device

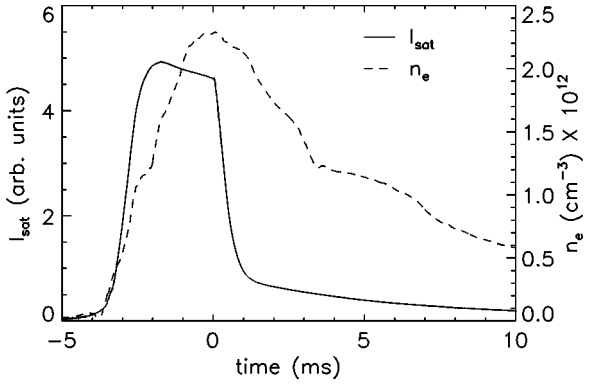

FIG. 2. Global time evolution of plasma parameters in absence of heating beam. The solid curve is the ion saturation current measured by a Langmuir probe at the center (axial and radial) of the large plasma column. The dashed curve is the electron density measured with a microwave interferometer. Discharge current $\sim$ 2.5 kA, $B_0=1$ kG. Transport experiments are performed during the afterglow phase ($t>0$) after the discharge current is shut-off.

(radial heat transport of the main plasma column is negligible because a/L is large) and eventually by cooling due to energy transfer to the ions (an important process for $T_e < 1.5$ eV). After the discharge is terminated the plasma density decays slowly (on a time scale of 2 ms) due to ambipolar flow at the sound speed.

The low ambient temperatures achieved during the afterglow stage considerably simplify the implementation of the heat transport experiment. For instance, when power densities, Q_b, on the order of $0.2\,\mathrm{W/cm^{-3}}$, are applied to afterglow plasmas in which the ambient electron temperature decays to a low level of $T_e \lesssim 1$ eV at densities $n \sim 2 \times 10^{12}\,\mathrm{cm^{-3}}$, it is possible to locally increase T_e by 2–10 times the ambient values. This implies that sizeable heat transport changes can be investigated using relatively modest electron-beam parameters. In fact, these very significant heating conditions can be achieved with small electron beams of low voltage (<20 V) at typical current levels of 200 mA. The low T_e values in the afterglow also imply relatively short mean-free path lengths thus permitting a clear study of the axial heat conduction features in regions well separated from the ends of the plasma device.

An important consequence of the low beam voltage required for meaningful studies is that the extra ionization produced by the beam electrons is negligible for the He conditions used. This implies that complicating features mixing plasma production and heating are absent in these experiments.

The heat source generator consists of a small electron beam 3 mm in diameter (comparable to the electron skin-depth) produced by biasing a heated, single crystal of lanthanum–hexaboride (LaB_6) with negative polarity relative to the mesh anode. The beam-generating crystal is located 75 cm from the end of the plasma column (i.e., 9.25 m from the cathode).

Figure 3 provides a schematic that illustrates the different regions of behavior of relevance to the transport studies and their relative spatial location within the plasma chamber. Typically a 20 V beam is injected at the radial center ($r = 0$) of the plasma column at an axial position near the electrically floating end of the device. Within 1 meter from the injection point the beam is completely thermalized. We envision this region to be an idealized heat source a few millimeters in diameter having a power density Q_b. Heat flows simultaneously along and across the ambient magnetic field from this source region and generates an expanding heat plume whose properties are measured at selected axial locations indicated in Fig. 3 by the arrows at values z_j. At the closest axial location z_1 (about 3 meters from the beam injector) the temperature filament exhibits large temperature increases on axis and a relatively narrow radial temperature profile (~ 1 cm). At a distant axial position z_3 (about 5 meters from the heat source) one observes small temperature increases and broad temperature profiles (~ 3 cm wide). Beyond z_4 (7 meters) there is no observable change in the ambient electron temperature.

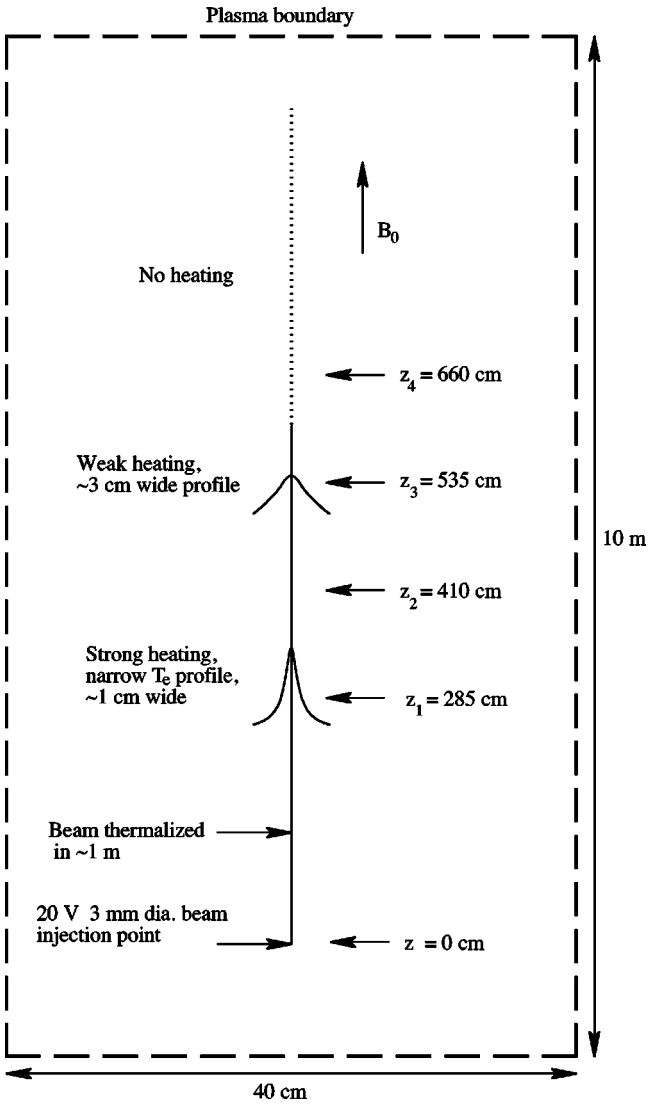

FIG. 3. Qualitative overview illustrating the spatial arrangement prevailing in the transport experiment. Axial locations z_j indicate where planes of Langmuir probe data are taken to sample the electron temperature.

III. DIAGNOSTIC TECHNIQUES

The electrons emitted from the beam cathode are slowed down and thermalized in a fairly short distance due to collisions with the bulk plasma electrons and ions. This slowing down process is represented by the Fokker–Planck equation.[4] The beam electrons can be considered as fast test particles interacting with slow bulk particles. Under these conditions the slowing down frequency for the beam electrons can be written as[4,5]

$$\nu_s^{e/\beta} = (1 + m_e/m_\beta)\frac{2\pi e^4}{\sqrt{2m_e}} E_b^{-3/2} n_e \lambda, \tag{3.1}$$

where e is the electron charge, m_β the mass of the plasma particle with which the beam electrons are colliding, E_b is the beam energy, n_e the density of the bulk plasma, and λ the Coulomb logarithm. Under the conditions of the experiments reported here ($n_e = 2.25 \times 10^{12}\,\mathrm{cm^{-3}}$), the 20 V beam electrons are slowed down in a distance of 70 cm. Further-

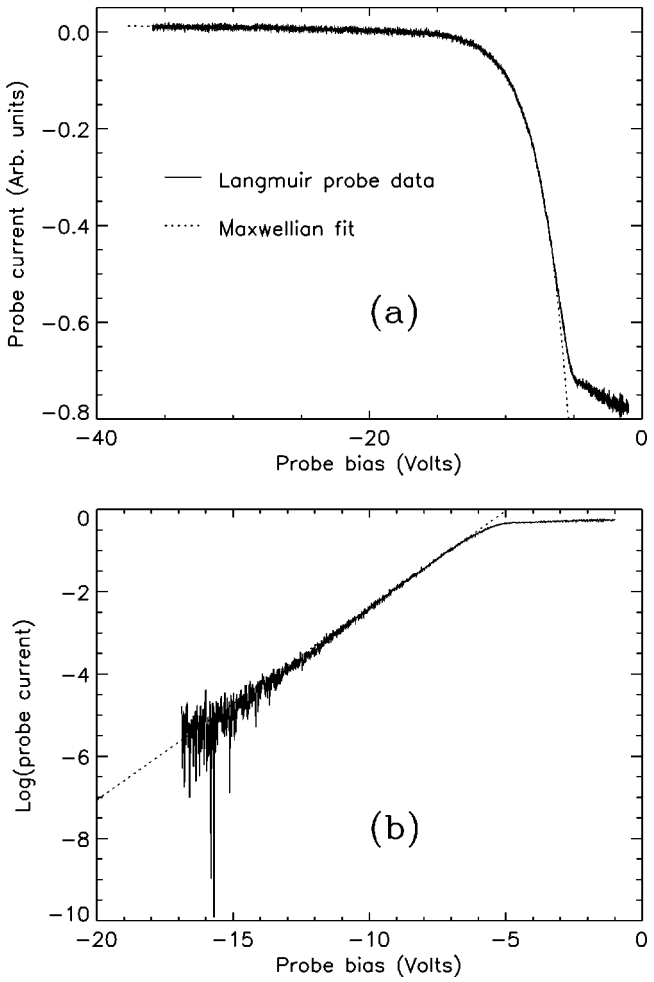

FIG. 4. (a) Current–Voltage (I–V) characteristic of a swept Langmuir probe (solid curve) at an axial position $z=285$ cm in the radial center of the temperature filament ($r=0$). The dotted curve is an exponential functional fit. (b) A semi-log plot demonstrating that the electron distribution function corresponds to thermal equilibrium conditions.

more, the energy of the injected beam is well below the ionization energy of neutral helium (24.46 eV) and also below the 21.22 eV energy needed to reach the $2\ ^1P$ state, the first excited state accessible from the ground state.[6] The 20 V beam energy is barely enough near the injection point (before slowing down) to reach the metastable $2\ ^3S$ (19.72 eV) state, so some few excited metastable neutrals may be created. However, we do not expect, and indeed do not observe ionization due to the injected beam. Thus, the role of the beam is to create an extended, rod-shaped heat source, from which heat is then conducted into the plasma due to Coulomb collisions of the Maxwellian bulk plasma. In our analysis of the heat conduction we model the heat source as a cylindrical region starting at the beam injection location, with a radius comparable to the estimated beam radius (2.5 mm), a length comparable to the slowing down distance (1 m), and having a constant power density (equal to the beam input power divided by the volume of the model heat source cylinder).

At a distance of 285 cm from the beam injection point the plasma is measured to be Maxwellian. Figure 4(a) shows an I–V trace obtained from a small (~ 1 mm^2) flattened-tip Langmuir probe in the center of the beam-heated plasma fitted to an exponential $[-A\exp(-V/T)]$ together with a linear ramp $(-bV)$ to match the trace in the ion saturation region ($V<floating\ potential$) of the curve. For purposes of assessing the degree to which the distribution is Maxwellian the fit is shown as a semi-log plot in Fig. 4(b) where the Maxwellian exponential appears as a straight line. The temperature of this clearly Maxwellian distribution is found to be 2.2 eV.

Using I–V traces from Langmuir probes has the advantage that the temperature, density, and plasma potential can be obtained. The principal disadvantage of this technique in the present study is that it takes a finite time interval to obtain the curves due to the requirement of a voltage sweep. Also the great variation in temperature from outside the heated filament where the plasma may be a few tenths of an eV to inside the filament where the temperature is several eV requires different sweep rates for optimal measurement. While a rapid sweep rate of several volts per microsecond can be used in the hot regions, the cold plasma region requires sweep rates of a few tenths of a volt per microsecond. Thus it takes about a hundred microseconds to measure the temperature using voltage sweeps, so that it is not possible to easily discern changes in temperature or density with this technique.

This difficulty can be overcome by using ion saturation current as a measure of the electron temperature. In plasmas with $T_i \lesssim T_e$, the ion saturation current is insensitive to T_i[7] and can be taken as proportional to $n_e T_e^{1/2}$. Thus the electron temperature can be measured using ion saturation current if the plasma density can be determined by other means. Since the beam does not produce ionization, the plasma density in the beam heated filament region can be taken to be equal to the density in the center of the plasma column. We determine the density of the plasma column by using the phase shift measured by a 56 GHz interferometer[8] located a distance 130 cm from the beam injection point. The interferometer measures a column average plasma density. Langmuir traces are used to obtain a relative density profile of the column which is then used in conjunction with the interferometer data to obtain a calibrated density profile across the column. The interferometer gives a continuous readout of the phase shift so that instantaneous column averaged density measurements are available.

In the study of heat transport in the filament we use the following expression for the electron temperature:

$$T_e(\vec{r},t)=T_e^0\left(\frac{I_{\rm sat}(\vec{r},t)}{I_{\rm sat}^0}\right)^2\left(\frac{n_e^0}{n_e(t)}\right)^2, \tag{3.2}$$

where the calibration parameters $I_{\rm sat}^0$, T_e^0, and n_e^0 correspond to measurements at a single time and location. Typically, the calibration parameters are measured just before beam turn on. The continuous plasma density $n_e(t)$ is obtained from the 56 GHz interferometer. Figure 5 shows a comparison between temperature measurements obtained using swept Langmuir voltage traces and those obtained from Eq. (3.2) using ion saturation measurements. The two curves agree over most of the temperature range sampled to within experi-

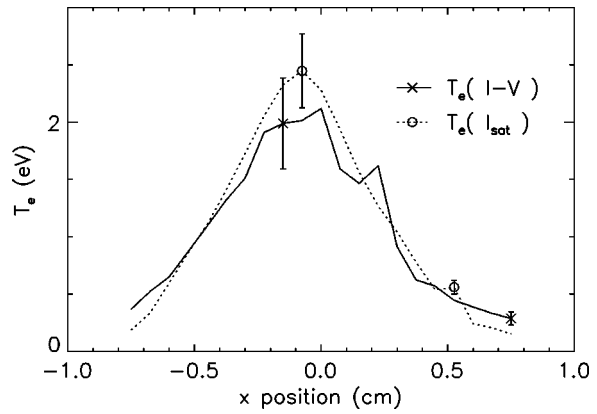

FIG. 5. A comparison of a voltage-swept Langmuir probe measurement (solid line) of the filament temperature profile with a calibrated ion saturation current (I_{sat}) measurement (dotted line). The degree to which these curves agree indicates the accuracy of the I_{sat} measurement method used in the heat transport studies.

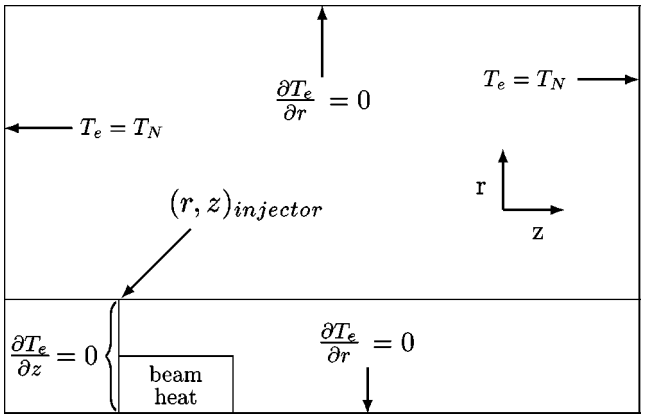

FIG. 6. Schematic of the two-dimensional geometry used in the transport code and associated boundary conditions. The confining magnetic field points along the *z*-direction.

mental error. The temperature measurements used in this study were obtained using the ion saturation current technique described here.

IV. HEAT TRANSPORT CODE

To achieve a detailed quantitative test of the predictions of the classical theory of heat transport in a magnetized plasma a time dependent, two-dimensional, nonlinear, heat transport code has been developed that incorporates realistic boundary conditions of relevance to the geometry of the experimental setup. The mathematical description does not contain the effects associated with convection and density changes. Since the agreement found between the code predictions and the experimental observations (discussed in detail in Sec. V) is within the experimental uncertainties, the role of these effects in the present quiescent environment is considered negligible.

The evolution of the electron temperature T_e is described by

$$\frac{3}{2}n\frac{\partial T_e}{\partial t} = \frac{1}{r}\frac{\partial}{\partial r}\left[r\kappa_\perp \frac{\partial T_e}{\partial r}\right] + \frac{\partial}{\partial z}\left[\kappa_\parallel \frac{\partial T_e}{\partial z}\right] - 3\frac{m}{M}\frac{n}{\tau_e}(T_e - T_i) + Q_b, \tag{4.1}$$

in which the ion temperature T_i is self-consistently calculated from

$$\frac{3}{2}n\frac{\partial T_i}{\partial t} = \frac{1}{r}\frac{\partial}{\partial r}\left[r\kappa_{\perp i}\frac{\partial T_i}{\partial r}\right] + 3\frac{m}{M}\frac{n}{\tau_e}(T_e - T_i) - 3n(T_i - T_0)n_0\sigma_0\left(\frac{T_i}{M}\right)^{1/2}, \tag{4.2}$$

where m, M refer to the electron and ion mass, respectively. In Eqs. (4.1) and (4.2) t is the time and (r,z) correspond to cylindrical coordinates with the z-axis along the confining magnetic field B_0. The phenomena under consideration is assumed to be cylindrically symmetric in zeroth-order; of course, when fluctuations develop this symmetry is destroyed.

The electron heat conduction coefficients in the axial and transverse direction appearing in Eq. (4.1) are those predicted by classical theory,

$$\kappa_\parallel = 3.16\frac{n_e T_e \tau_e}{m_e}, \qquad \kappa_\perp = 1.47\frac{\kappa_\parallel}{(\Omega_e\tau_e)^2}, \tag{4.3}$$

where $\Omega_e = eB_0/mc$, and $\tau_e = (3.44\times10^5)T_e^{3/2}/(n\lambda)$, with λ the usual Coulomb logarithm.

The corresponding transverse ion heat conductivity is given by

$$\kappa_{\perp i} = 2nT_i/(M\Omega_i^2\tau_i), \tag{4.4}$$

where $\tau_i = (2.09\times10^7)\sqrt{M/m_p}\,T_i^{3/2}/(n\lambda)$ and m_p is the proton mass; $\Omega_i = eB_0/Mc$.

In addition to the axial and transverse heat conduction processes, Eq. (4.1) contains the local heat loss experienced by the electrons due to the energy transfer to the ions by Coulomb collisions. The heat source Q_b is associated with the injection of the electron beam, and as indicated in Fig. 3, it is localized to a region approximately 1 meter in extent where thermalization of the injected beam occurs.

The ion temperature equation [Eq. (4.2)] contains the effect of transverse ion heat conductivity and neglects the axial heat conduction (it is insignificant). This equation also contains the important local coupling to the electrons by Coulomb collisions as well as direct local cooling caused by the ambient neutral He gas that remains within the chamber and having density n_0 and temperature T_0. σ_0 is the ion–neutral collision cross section.

The coupled equations (4.1) and (4.2) are solved numerically using the standard algorithm[9] for equations of this type based on the alternating-direction implicit method. The self-adjoint form of the spatial derivative is preserved by the tri-diagonal scheme employed.

The boundary conditions implemented in the transport code are illustrated in Fig. 6. At the extreme ends of the plasma column the electron and ion temperatures are set equal to the neutral temperature, $T_e = T_i = T_0$ (cathode temperature, i.e., 0.15 eV). At the column center ($r = 0$) and at the far radial boundary (10 times the beam size) the derivative of the electron and ion temperatures is set to zero, i.e., $\partial T_j / \partial r = 0$. Since the support structure associated with the beam injector intersects field lines that connect to the region where beam thermalization occurs, the heat that flows along those lines does not reach the end plate. In fact, because the structure is biased negatively it reflects most of the electrons and its behavior is thus modeled as a perfect heat reflector. This feature is implemented by legislating that at the axial position where the injector is located $\partial T_e / \partial z$ is set to zero within radial distances $r < r_i$ where r_i is the transverse dimension of the injector, which is larger than the transverse dimensions of the injected beam, and of the associated heat source, Q_b.

The heat source Q_b is modeled as a uniform region of radius a and length L_s starting at the axial location of the beam injector. The numerical value of Q_b is determined by equating the total power in the idealized heat source to the actual injected power of the beam, i.e., $Q_b \pi a^2 L_s = I_b V_b$, where I_b is the measured beam current and V_b the measured beam voltage. In the quantitative comparison with experimental results L_s is taken to be 1 meter (comparable to the predicted thermalization length) and $a = 0.25$ cm, the estimated source radius. It should be noted that the inherent uncertainty in estimating the quantity L_s is not significantly different from the theoretical uncertainty associated with the truncation effect of the Coulomb logarithm, which for comparison studies reported in Sec. VI is taken as $\lambda = 12.0$, based on the values of typical ambient parameters.

The individual components of the code, i.e., radial transport and axial transport, were benchmarked against test cases using constant heat conductivities. In addition, the full code was compared with predictions of an effective ''local code'' in which the spatial derivatives were replaced by effective scale lengths. It is found that both methods yield results that agree within the expected limitations of the heuristic local approximation. Sensitivity studies were also performed to check the dependence of numerical stability and accuracy of the results on the choice of the temporal and spatial step-size. It is found that for the parameters of relevance to the experiments a time step of 1 μs and a 128 by 128 spatial mesh with physical dimensions $\Delta r = 3$ cm, $\Delta z = 1000$ cm provides an excellent compromise between reliability and speed of execution.

Next we proceed to illustrate the capabilities of the transport code and to elucidate some of the nontrivial predictions of classical theory that are inherently present in realistic laboratory studies of two-dimensional heat transport in magnetized plasmas.

Figure 7 displays the predicted temporal evolution of the axial temperature profile for a case in which the heat source (in practice the electron beam) is turned on at a time (defined as $t = 0$) when the electrons in the background plasma have reached a temperature $T_e = 1.5$ eV during the afterglow phase. The radial position corresponds to $r = 0$. This figure illustrates a rather nonintuitive behavior of the heat pulse. Early in time (the curve marked 0.01 ms) T_e increases rapidly in the vicinity of the heat source location where $Q_b \neq 0$ ($75\,\text{cm} < z < 175\,\text{cm}$). The remainder of the temperature profile is the cooling afterglow bulk plasma. As the shape of the plume evolves the value of the aspect ratio a/L decreases below the critical value at which the radial losses become larger than the axial losses. The effect is clearly visible in Fig. 7. The leading edge of the temperature plume retreats between time $t = 0.2$ ms and $t = 1.0$ ms. This effect results in a clear signature at axial location $z = z_2$ where the temperature reaches a maximum and then decreases. This dynamical retreat of a heat plume is an intrinsic feature of the classical theory of heat transport in a magnetized plasma that provides a unique signature amenable to experimental study.

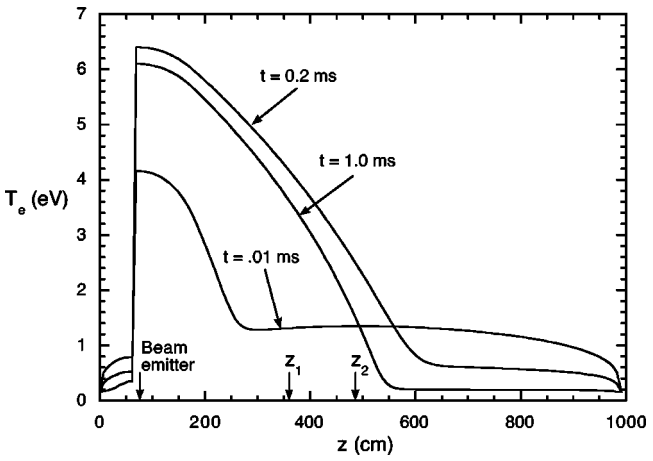

FIG. 7. Axial dependence of electron temperature at the center of temperature filament ($r = 0$) for different times after the heating beam is turned-on ($t = 0$). Results are predictions of the two-dimensional code. Note the retreat of the temperature plume between $t = 0.2$ ms and $t = 1.0$ ms.

To better elucidate the two-dimensional character of the evolving temperature filament Fig. 8 displays contours of constant T_e in the r-z plane for different times after the heat source is turned on. It should be noted that in this figure the axial scale is compressed by a factor of 500 in order to resolve the narrow transverse variations. The spacing of the temperature contours shown corresponds to 0.5 eV. In order to illustrate the important dependence of classical heat transport on the strength of the confining magnetic field the top three panels in Fig. 8 display the evolution at a large field value (1.5 kG) while the bottom panels correspond to a lower value (0.75 kG). It is clearly seen that at lower values of B_0 the heat plume is relatively wider than at large B_0 and accordingly the length of the temperature filament is much larger at larger B_0. Again, these are characteristic signatures that can be experimentally tested.

V. EXPERIMENTAL RESULTS

The experimental tests of the classical theory of heat transport consist of direct comparison of the measured electron temperature, consistently deduced from Langmuir probe data, with the predictions of the transport code described in

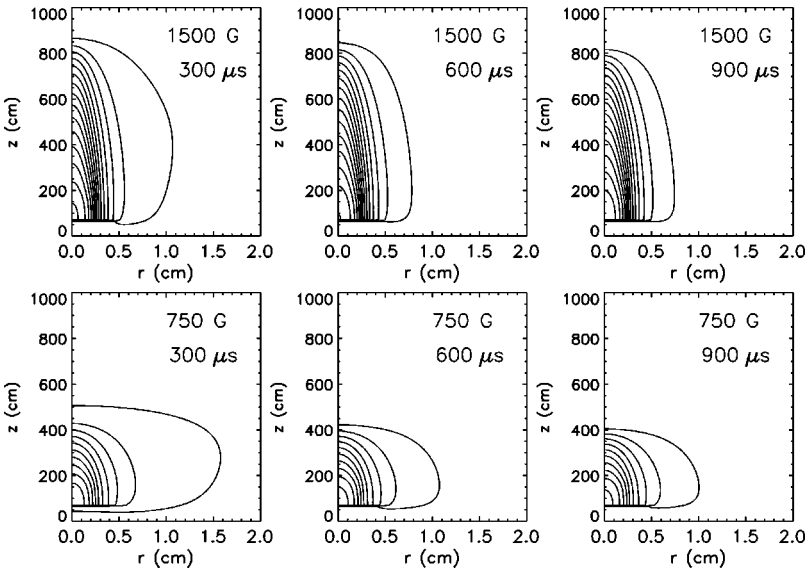

FIG. 8. Time evolution of two-dimensional contours (in *r-z* coordinates) of electron temperature predicted by the transport code for two different values of the confining magnetic field. Top panel: $B_0=1.5$ kG. Bottom panel: $B_0=0.75$ kG. The axial scale is contracted by a factor of 500.

Sec. IV for various conditions. The comparison considers the full time evolution of the temperature filament at various axial positions over a range of temperature increases ($\delta T_e/T_e\sim$ 1–10) in which the different nonlinear dependences of $\kappa_\parallel$ and $\kappa_\perp$ on T_e are sampled. The tests also probe the radial temperature profile and the dependence of the phenomena on the strength of the confining magnetic field over a factor of 3 (a factor of 9 variation in $\kappa_\perp$).

Figure 9 displays the time evolution of the electron temperature profile at the center of the temperature filament ($r=0$) for two different axial positions $z_1=285$ cm, $z_2=410$ cm away from the beam injector (as sketched in Fig. 3). The strength of the confining magnetic field is 1 kG for this case. The solid curves correspond to experimental measurements and the dashed and dotted curves are the predictions of the transport code. The dashed curve neglects the effects of radial conduction (i.e., $\kappa_\perp=0$), hence it succinctly depicts the role of field-aligned thermal conduction. The dotted curve is the fully 2-dimensional result in which $\kappa_\parallel$ and $\kappa_\perp$ are both retained and given by Eq. (4.3).

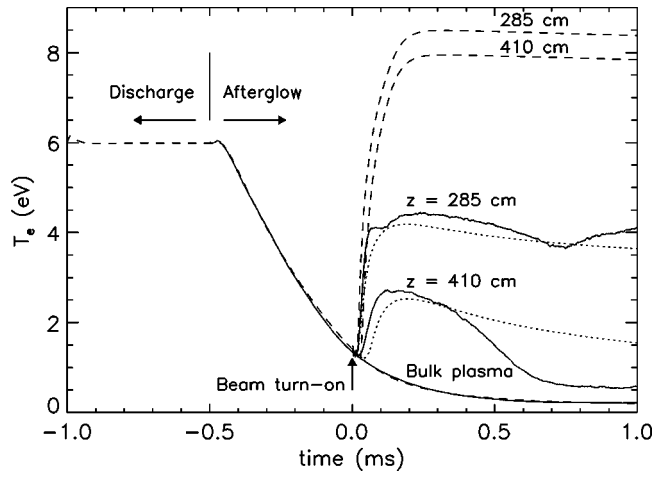

FIG. 9. Time evolution of electron temperature over a time span including the discharge and afterglow stages. The heating beam is turned on at $t=0$. The solid curve is the measured electron temperature at the center of the temperature plume ($r=0$). Behavior at two different axial positions: $z_1=285$ cm and $z_2=410$ cm are shown. The dashed curve is the result of the transport code with $\kappa_\perp=0$ (1-D). Dotted curves are predictions of the 2-D code based on classical heat conductivities. $B_0=1$ kG.

The time interval displayed in Fig. 9 spans a range of 2.0 ms. For $t<-0.5$ ms the discharge current is on and a steady-state temperature of 6 eV is achieved. This temperature is determined by a balance between axial heat losses to the end of the machine and the Ohmic heating associated with the discharge current. The role of radial heat transport is negligible during this stage because the aspect ratio a/L of the plasma column is larger than the critical value described previously. In the interval $t<-0.5$ ms Fig. 9 only displays the dashed curve corresponding to the prediction of the one-dimensional (1-D) transport code; the measured value of T_e overlaps this line, but for clarity of presentation it is not shown. However, it must be emphasized that the transport code based on classical heat conduction along the axial direction is in full quantitative agreement with the measured behavior of the steady-state discharge.

It is seen from Fig. 9 that at $t=-0.5$ ms the discharge current is turned-off and the plasma enters the afterglow phase. It should be noted that the measured decay in T_e is also well described by the 1-D transport code over the entire decay stage extending up to $t=1.0$ ms and labeled as ''bulk plasma.'' This trace corresponds to the baseline conditions prevailing in the absence of the heat input provided by the injected beam.

The heat resulting from beam injection ($I_b=220$ mA, $V_b=20$ V) at $t=0$ is represented in Fig. 9 by the rapidly rising solid curves. It is seen that these curves closely overlap the predicted behavior of the 2-D transport code (dotted curves) and display the characteristic drop associated with the retreat of the heat plume described in Sec. IV and illustrated in Fig. 7. It is also seen in Fig. 9 that radial heat transport plays a crucial role in determining the observed behavior. The dashed curves obtained with $\kappa_\perp=0$ fail to predict the saturation level, and do not exhibit the characteristic retreat. However, the $\kappa_\perp=0$ code explains correctly the

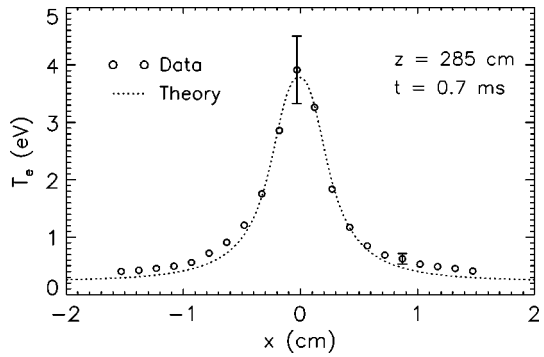

FIG. 10. A comparison of measured electron temperature profile (open symbols) in the direction transverse to the confining magnetic field with the prediction of classical transport code (dotted curve). $B_0=1$ kG. Heat source is turned-on at $t=0$.

measured behavior of the large-scale plasma column in which the aspect ratio a/L is larger than the critical value previously discussed. This implies that the controlled injection of heat at a small transverse scale is found to simultaneously expand across and along the confining magnetic field at the different rates predicted by the intrinsically anisotropic classical theory of transport based on Coulomb collisions in a magnetized plasma.

Having ascertained the predicted temporal behavior at two distant axial positions at the center of the temperature filament $(r=0)$ the question remains as to how well is the observed radial temperature profile explained by classical theory. The relevant comparison is shown for $B_0=1$ kG in Fig. 10 at an axial position $z=285$ cm away from the beam injector at a time $t=0.7$ ms after the heat source is turned-on (the full time dependence at $r=0$ is shown in Fig. 9). In this figure the dotted curve is the predicted behavior of the 2-D transport code and the open symbols are experimental measurements which scan the full spatial dependence across the temperature filament on both sides of its center, hence the x-label used in this display. It is found from Fig. 10 that within the experimental uncertainty the measured temperature profile is well described by the classical theory.

The sensitivity of the predicted temporal and spatial behavior of the temperature plume to the numerical coefficients of the perpendicular and parallel heat conductivities given in Eq. (4.3) are illustrated in Fig. 11. If the numerical coefficient of $\kappa_\perp$ is doubled the heat transport code predicts, at t = 1 ms, a filament two meters shorter with a peak temperature at position z_1 (285 cm) less than half the classical value. On the other hand, if $\kappa_\perp$ is halved, the filament is three meters longer and the peak temperature at z_1 is almost double the classical value. Clearly the predicted spatial distribution of the temperature is very sensitive to the value of the numerical coefficient of $\kappa_\perp$. The numerical coefficient of $\kappa_\perp$ must be within 10% of the classical value to agree with the measurements. Changing the coefficient of $\kappa_\parallel$ results mostly in a change in the axial temperature gradient. Doubling the numerical coefficient of $\kappa_\parallel$ results in a filament about a meter longer with a gentler temperature gradient and the temperature at z_1 remains essentially unchanged while the temperature at z_2 increases. Halving the numerical coefficient of $\kappa_\parallel$

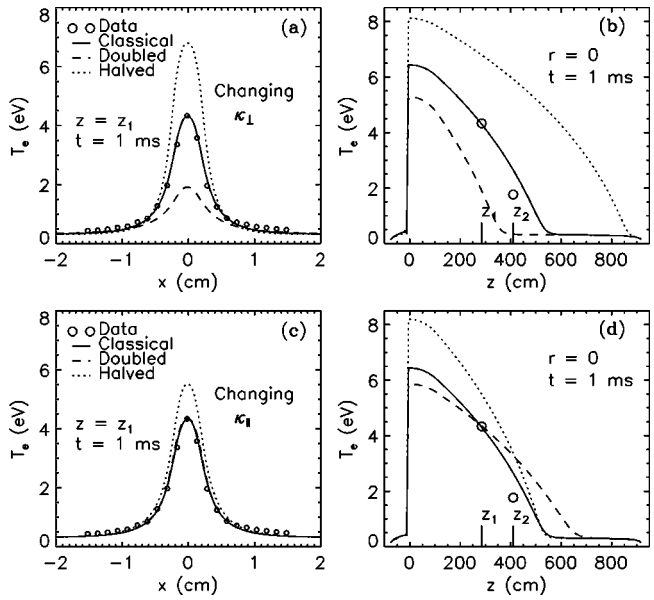

FIG. 11. Predictions of the transport code compared to experimental data points for various values of the numerical coefficient of $\kappa_\perp$ and $\kappa_\parallel$. Results of doubling and halving the coefficient of $\kappa_\perp$ are shown in (a) and (b) while the results of doubling and halving the coefficient of $\kappa_\parallel$ is shown in (c) and (d).

produces a filament about the same length but with a steeper gradient than the classical value. As a result, the temperature at z_1 is increased by about 20%, while the temperature at z_2 increases by 30%.

To explore the role played by the ions in determining the shape of the measured radial electron temperature profile, Fig. 12 compares the predictions of the 2-D code for three different ion models. The electron temperature is represented by the open circles and correspond to measurements at $z=285$ cm at $t=0.7$ ms. The dotted line is the prediction based on local ion cooling by neutrals alone, i.e., $\kappa_{\perp i}=0$. The constant dash-length curve is obtained by holding the ion temperature constant, while the dash–dot curve represents the prediction including local ion cooling and ion cross-field conduction, as given by Eq. (4.4). From an exami-

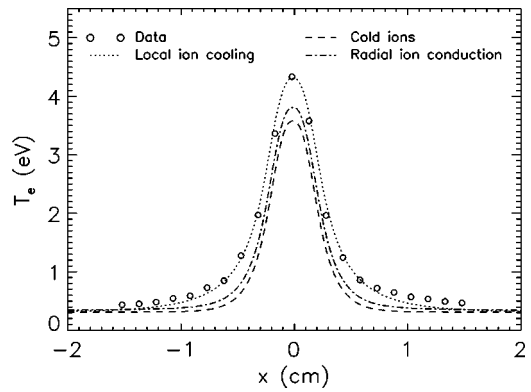

FIG. 12. The role of ion behavior in determining the electron temperature profile for $B_0=1$ kG. Open symbols are experimental measurements. The dotted curve is obtained by local ion cooling model; the dashed curve is the result of holding the ion temperature constant, and the dot–dashed curve uses classical ion thermal conduction as given by Eq. (4.4).

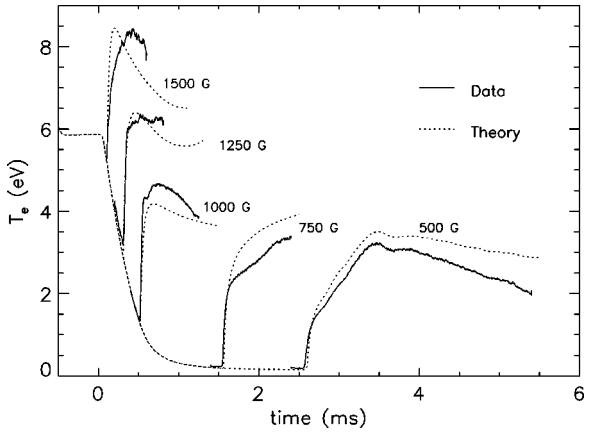

FIG. 13. Time evolution of the electron temperature at $r=0$, $z=285$ cm for different values of the confining magnetic field. Solid curves are measurements and dotted curves are predictions of classical transport theory. The turn-on time for the heating beam is different for the different field strengths to ensure quiescent conditions.

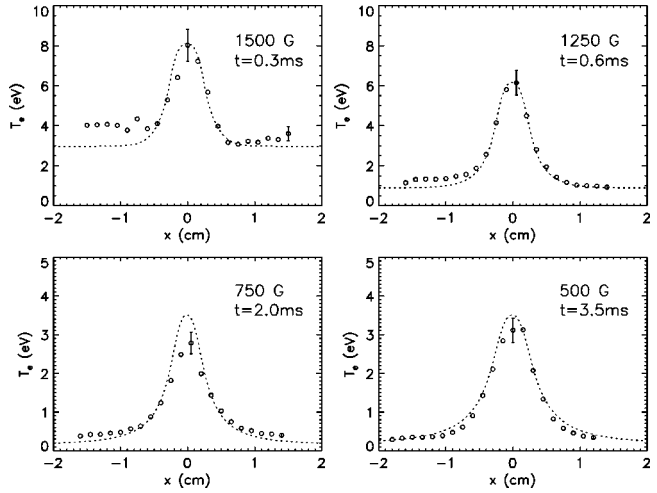

FIG. 14. Electron temperature profiles transverse to the confining magnetic field for different field strengths. Open symbols are measurements and dotted curves are predictions of classical theory. The time marks correspond to the time scale in Fig. 13.

nation of Fig. 12 it can be deduced that the local model, in which the ion temperature achieves a higher value, provides a better fit to the measured behavior. It can also be deduced that holding the ions at constant temperature gives the worst agreement and that the inclusion of $\kappa_{\perp i}\neq 0$ is somewhere in between. However, it must be realized that the ion contribution to the T_e profile is relatively small and the differences between the three ion models is within experimental uncertainty. Since in this study there is no independent measurement of the ion temperature it would be inappropriate to conclude the existence of an anomaly in the ion behavior. However, it must be mentioned that the best fit to the entire data set gathered in this study (including results not presented here) is consistently obtained by using the local ion cooling model.

The dependence of the behavior of heat transport on the strength of the confining magnetic field is illustrated in Fig. 13. The results shown in this figure are analogous to those presented in Fig. 9 for $B_0=1$ kG. A significant difference in Fig. 13 is that the time at which the heating beam is turned on during the afterglow stage is different for the different values of magnetic field used. One reason for doing this is to ensure that the relevant data pertains to a quiescent situation in which spontaneous fluctuations do not play a role in the transport processes. The position along the temperature filament being sampled in Fig. 13 is $r=0$ and $z=285$ cm. The solid curves correspond to measured values of the electron temperature and the dotted curves are the predictions of the 2-D transport code for the different values of B_0 in the range of 0.5 kG to 1.5 kG. It is seen from Fig. 13 that the observed temporal evolution of the temperature filament closely follows the predicted behavior, including the rise time, saturation, and characteristic retreat features. This close agreement is quite remarkable because it corresponds to a variation of a factor of 9 in $\kappa_\perp$, with no change in $\kappa_\parallel$. Of course, because $\kappa_\perp$ and $\kappa_\parallel$ have a different functional dependence on T_e the different curves in this figure also validate the correct temperature dependence associated with the classical theory of heat transport.

The radial profiles of T_e corresponding to the different values of the confining magnetic field are shown in Fig. 14 for an axial position $z=285$ cm from the beam injector. The times indicated in the various panels correspond to the time scale used in the display of Fig. 14. It is seen from Fig. 14 that good agreement is obtained between the measured values of T_e (open symbols) and the predictions of the 2-D code (dotted curves). However, at the larger magnetic field values a noticeable departure from the predicted behavior begins to occur. The reason for these small departures from classical behavior can be traced to the presence of a finite level of enhanced fluctuations, which for the higher magnetic field cases develop very early in time and thus can not be fully eliminated by a judicious choice of the beam turn-on time. The overall trend seen from the profiles in Fig. 14 is that as B_0 is decreased the temperature changes achieved are smaller and the profiles are wider, as expected.

Figure 15 documents the development of spontaneous

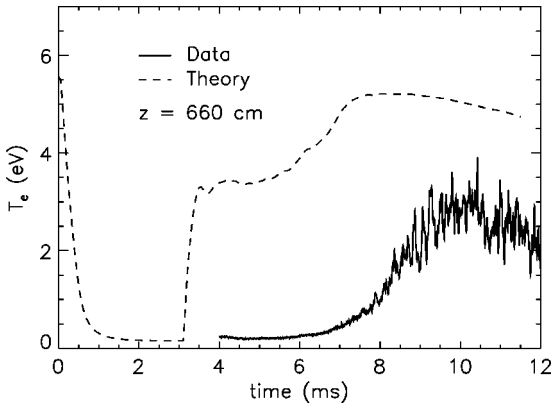

FIG. 15. Time evolution of electron temperature data (solid curve) at $r=0$, $z=660$ cm shows development of spontaneous fluctuations on a longer time scale for $B_0=1$ kG. The dashed curve is the behavior predicted by the classical theory of heat transport, which in the presence of fluctuations fails to explain the observed behavior. To be compared to quiescent behavior shown in Fig. 9.

fluctuations and the associated departure from the behavior predicted by classical theory at a location $r=0$, $z=660$ cm, for $B_0=1$ kG. The solid curve corresponds to measured values of T_e; it clearly shows the spontaneous development of fluctuations in a frequency range $\omega \lesssim 0.1\Omega_i$. The dashed curve is the prediction of the 2-D transport code which in this case fails to explain the observed behavior. We defer the study of the fluctuations and the transition to anomalous heat transport to a future detailed publication. The purpose of showing the result of Fig. 15 is to document that in this study the failure of the classical theory of transport is indeed sampled when conditions that result in steep temperature gradients are achieved, as is natural at the higher values of the confining magnetic field which result in a situation, albeit short-lived, of smaller radial heat conduction.

VI. CONCLUSIONS

In this study we report measurements of electron heat transport from a carefully chosen experimental arrangement using the Large Plasma Device (LAPD) at UCLA that conclusively demonstrate the quantitative predictions of the classical theory of heat transport in a strongly magnetized plasma (i.e., electron gyrofrequency much larger than the Coulomb collision frequency, $\Omega_e \gg \nu_{ei}$). By comparing the experimental observations to the predictions of a two-dimensional, time dependent, nonlinear, transport code the nontrivial features associated with simultaneous transport along and across the magnetic field have been verified. The simultaneous nonlinearities of the transverse and axial conductivities have been probed over a range of temperature increases $\delta T_e/T_e \sim$ 1–10. The dependence on the confining magnetic field has been verified over a factor of three. It is found that under quiescent conditions the details of the measured spatio-temporal evolution and radial temperature profiles agree with the predictions of classical theory within the intrinsic uncertainties of the experimental arrangement.

In the study we have also identified the limitations of the classical theory. Over long time scales, or for conditions that result in very steep temperature gradients, as is natural for large confining magnetic fields, spontaneous fluctuations lead to significant departures from classical heat transport behavior.

There are several elements in this study that have facilitated the study of classical behavior. Foremost is the large dimension of the plasma device in relation to the region of elevated temperature being studied. For all practical purposes the geometry achieved corresponds to that of an expanding heat plume embedded in an infinite plasma. To sample the intrinsic anisotropic nature of the classical theory it is necessary for the temperature filament to meet the stringent requirement that $a/L < 1.72(\Omega_e \tau_e)^{-1}$. It is the essence of this experiment that this condition is achieved by using a beam of small transverse extent and a very long plasma. Complications resulting from secondary ionization produced by the injected beam have been mitigated by working at relatively low voltages. This capability has been facilitated by the usage of afterglow plasmas and relatively large confining magnetic fields, so that substantial heating can be achieved with modest heating power densities.

It should be emphasized that the past decade has seen the development of increasingly sophisticated experiments probing the nature of classical transport. Noteworthy among these are measurements of the effective cross-field thermal conductivity,[10] determination of velocity–space transport,[11] and test particle transport[12] in non-neutral plasmas. Most recently very delicate experiments[13] in non-neutral plasmas have observed large transverse heat diffusivities (compared to the classical values measured here) associated with the small Larmor radius conditions prevailing in such systems.

ACKNOWLEDGMENTS

Research performed by A. T. Burke and G. J. Morales is sponsored by the Department of Energy and the Office of Naval Research and that of J. E. Maggs by the Office of Naval Research and the National Science Foundation.

[1] L. Spitzer, Jr. and R. Härm, Phys. Rev. **89**, 977 (1953).
[2] S. I. Braginskii, in *Reviews of Plasma Physics*, edited by M. A. Leontovich (Consultants Bureau, New York, 1965), Vol. 1, p. 205.
[3] W. Gekelman, H. Pfister, Z. Lucky, J. Bamber, D. Leneman, and J. Maggs, Rev. Sci. Instrum. **62**, 2875 (1991).
[4] G. Schmidt, in *Physics of High Temperature Plasmas*, 2nd ed. (Academic, New York, 1979), pp. 375–387.
[5] D. L. Book, in *NRL Plasma Formulary*, NRL Publication 177-4405, Washington, DC, 1990, pp. 31–33.
[6] G. Herzberg, in *Atomic Spectra and Atomic Structure* (Dover, New York, 1944), pp. 64–66.
[7] F. F. Chen, in *Plasma Diagnostic Techniques*, edited by R. H. Huddlestone and S. L. Leonard (Academic, New York, 1965), Sec. 3.3, pp. 138–150.
[8] H. Hutchinson, in *Principles of Plasma Diagnostics* (Cambridge University Press, New York, 1987), pp. 95–115.
[9] W. H. Press, S. A. Teukolsky, W. T. Vetterling, and B. P. Flannery, *Numerical Recipes in C* (Cambridge University Press, New York, 1992), p. 856.
[10] D. D. Needelman and R. L. Stenzel, Phys. Rev. Lett. **58**, 1426 (1987).
[11] J. Bowles, R. McWilliams, and N. Rynn, Phys. Rev. Lett. **68**, 1144 (1992).
[12] F. Anderegg, X. P. Huang, C. F. Driscoll, E. M. Hollmann, T. M. O'Neil, and D. H. E. Dubin, Phys. Rev. Lett. **78**, 2128 (1997).
[13] E. M. Hollmann, F. Anderegg, and C. F. Driscoll, Phys. Rev. Lett. **82**, 4839 (1999).